

THE ISOTHERMAL OUTFLOW IN HIGH-MASS STAR-FORMING REGION G240.31+0.07

JUNHAO LIU and KEPING QIU

School of Astronomy & Space Science, Nanjing University, Nanjing, P.R.China

ABSTRACT

We present Atacama Pathfinder Experiment (APEX) observations of the massive star-forming region G240.31+0.07 in the CO (3-2), (6-5), and (7-6). The integrated high-velocity and low-velocity emissions of the three lines reveal a bipolar outflow and show similarity in morphology. Together with the combined data from the Submillimeter Array (SMA) and the Caltech Submillimeter Observatory (CSO) 10.4 m telescope in CO (2-1), we explore the physical conditions of the outflowing gas as a function of gas velocity, by the means of Large Velocity Gradient (LVG) modeling and population diagram analysis. Our results reveal that the temperature of the outflowing gas has an almost constant value of ~ 50 K. The constant trend is consistent with the isothermal assumption of the wide-angle wind model. We also find a decreasing trend of CO column density with gas velocity. In addition, the modeling results reveal that the outflowing gas is thermalized and no upper limits to the gas density could be derived. The lower limits of gas density are $n_{\text{low}} \sim 10^5 \text{ cm}^{-3}$ at most velocities.

Subject headings: ISM: individual (G240.31+0.07) - ISM: jets and outflows - stars: formation - stars: early-type

1. INTRODUCTION

Bipolar molecular outflows are ubiquitous around low-mass and high-mass young stellar objects (Lada 1985; Fukui et al. 1993; Zhang et al. 2001; Beuther et al. 2002; Maud et al. 2015). Theoretical works suggest that, for low-mass star formation, molecular outflows are related to disk-accretion processes, and play an important role in dissipating excess angular momentum of the infalling material (Shu et al. 1987; Bachiller 1996). However, due to the rarity and the typically larger distances, massive molecular outflows and their driving sources are not studied as well as their low-mass counterparts. Thus, it is unclear how the massive outflows are accelerated, how they differ from low-mass outflows, and how they affect the star-forming processes. It is essential to address these questions by studying individual high-mass star-forming regions.

Most previous studies of outflows have used low-excitation lines of CO, which are easily excited

at low temperatures, to characterize the relatively cold molecular gas in morphology and kinematics (Qiu et al. 2009; Qiu & Zhang 2009; Qiu et al. 2011). Deriving the physical conditions of the outflowing gas requires sensitive observations of CO across multiple transitions, while observations of high-J CO lines are very rare.

Here we report the 12-m submillimeter Atacama Pathfinder Experiment Telescope¹ (APEX) observations of G240.31+0.07 (hereafter G240), an active high-mass star-forming region which is associated with the young stellar object (YSO) IRAS 07427-2400 and located at a distance of 5.41 kpc (Sakai et al. 2015). It harbors an ultra-compact (UC) HII region and is associated with OH and H₂O masers (Hughes & MacLeod 1993; Caswell 1997; MacLeod et al. 1998; Migenes et al. 1999; Caswell 2003). Its far-infrared lumi-

¹The Atacama Pathfinder Experiment Telescope is a collaboration between the Max-Planck-Institut für Radioastronomie, the European Southern Observatory, and the Onsala Space Observatory.

osity of $10^{4.7} L_{\odot}$ is consistent with a spectral type O8.5 zero-age main-sequence (ZAMS) star (MacLeod et al. 1998). A near-infrared study has found two bright elongated H_2 emission knots near the source (Kumar et al. 2002). Kumar et al. (2003) further argued that the shocked H_2 emission indicates the presence of a massive rotating disk/envelope around the luminous YSO IRAS 07427-2400. There are also millimeter and centimeter radio continuum observations toward G240. Two clumps were detected by Chen et al. (2007) at 654 GHz ($460 \mu\text{m}$), with clump A coinciding with a VLA 6 cm point source (Hughes & MacLeod 1993) and an H_2O maser. Qiu et al. (2009) presented a high resolution interferometric study at 1.3 mm and resolved the central part of G240 into three dusty cores MM1, MM2, and MM3, with the brightest core MM1 coinciding with the VLA 6 cm point source spatially. Trinidad (2011) presented observations at 1.3, 3.6, and 6 cm and reported radio continuum emissions at the position of the three millimeter sources in at least one wavelength. G240 has also been mapped with single dish and interferometric observations in CO emission. High-velocity CO (1-0) gas was detected towards G240 (McCutcheon et al. 1991; Shepherd & Churchwell 1996), tracing a bipolar outflow (Shepherd & Churchwell 1996). Hunter (1997) mapped the CO (3-2) emission with a $20''$ beam and found a prominent bipolar outflow at a position angle (PA) of 138° and a weaker component at $PA \sim 101^\circ$. Kumar et al. (2003) also detected a prominent component and a weaker component of the bipolar CO (3-2) outflow with a $20''$ beam and reported the PA of the prominent component to be 132° . Recently, Qiu et al. (2009) presented a detailed single dish and interferometric study of $^{12}\text{CO}(2-1)$ and $^{13}\text{CO}(2-1)$ emission and detected a bipolar, wide-angle, quasi-parabolic molecular outflow. In addition, Qiu et al. (2014) reported the detection of an hourglass magnetic field aligned within 20° of the outflow axis.

In this paper, we present a CO multi-transition (3-2, 6-5, 7-6) study towards the G240 outflow. With large velocity gradient (LVG) calculations and population diagram analysis, we estimate the physical conditions of the outflowing gas as a function of outflow velocity. We then discuss the results of the analysis.

2. OBSERVATIONS

The APEX observations were conducted on . CO (6-5) and CO (7-6) were observed simultaneously. The pointing error was found to be and we have fixed it.

3. RESULTS

3.1. CO EMISSIONS

Figure 1 shows the maps of the integrated low-velocity (LV) and high-velocity (HV) blueshifted and redshifted emissions of CO $J = (3-2)$, (6-5), (7-6) lines. We integrate the LV and HV line wings of CO (3-2) and CO (6-5), as well as CO (7-6) LV emission, with the same velocity range as that in Figure 2(a) and Figure 2(b) of Qiu et al. (2009), which is from 58 to 64 km s^{-1} and from 74 to 80 km s^{-1} for the LV blueshifted lobe and redshifted lobe, from 42 to 56 km s^{-1} and from 82 to 94 km s^{-1} for the HV blueshifted lobe and redshifted lobe, respectively. As the CO (7-6) observation is less sensitive than observations of CO (3-2) and CO (6-5), we integrate the HV emission of CO (7-6) from 50 to 56 km s^{-1} for the blueshifted lobe and from 82 to 88 km s^{-1} for the redshifted lobe, to exclude channels which are dominated by noise. The outflow morphologies seen in three lines are very similar. For CO $J = (3-2)$ and (6-5) emissions, a low-velocity and high-velocity prominent bipolar outflow is detected at position angle (PA) $\sim 131^\circ$, along with a low-velocity weaker component detected at $PA \sim 101^\circ$. However, the weaker outflow is not clearly seen in CO (7-6). It could result from the limited sensitivity of CO (7-6) observation. Due to the low resolution of our CO $J = (3-2)$, (6-5), (7-6) observations, we don't see the wide-angle structure reported by Qiu et al. (2009).

3.2. LINE RATIOS

For a proper comparison of different line emissions, we convolved the CO (6-5) and (7-6) maps, as well as the CO (2-1) map from Qiu et al. (2009), to the same spatial resolution of CO (3-2), which is $19''$. To reduce the noise level, we resampled the four CO lines to the resolution of 2 km s^{-1} . Then we measured the main beam temperature ratios of the four transitions toward the peak of the blueshifted and redshifted lobes (marked as two crosses in Figure 1). We adopted the cloud

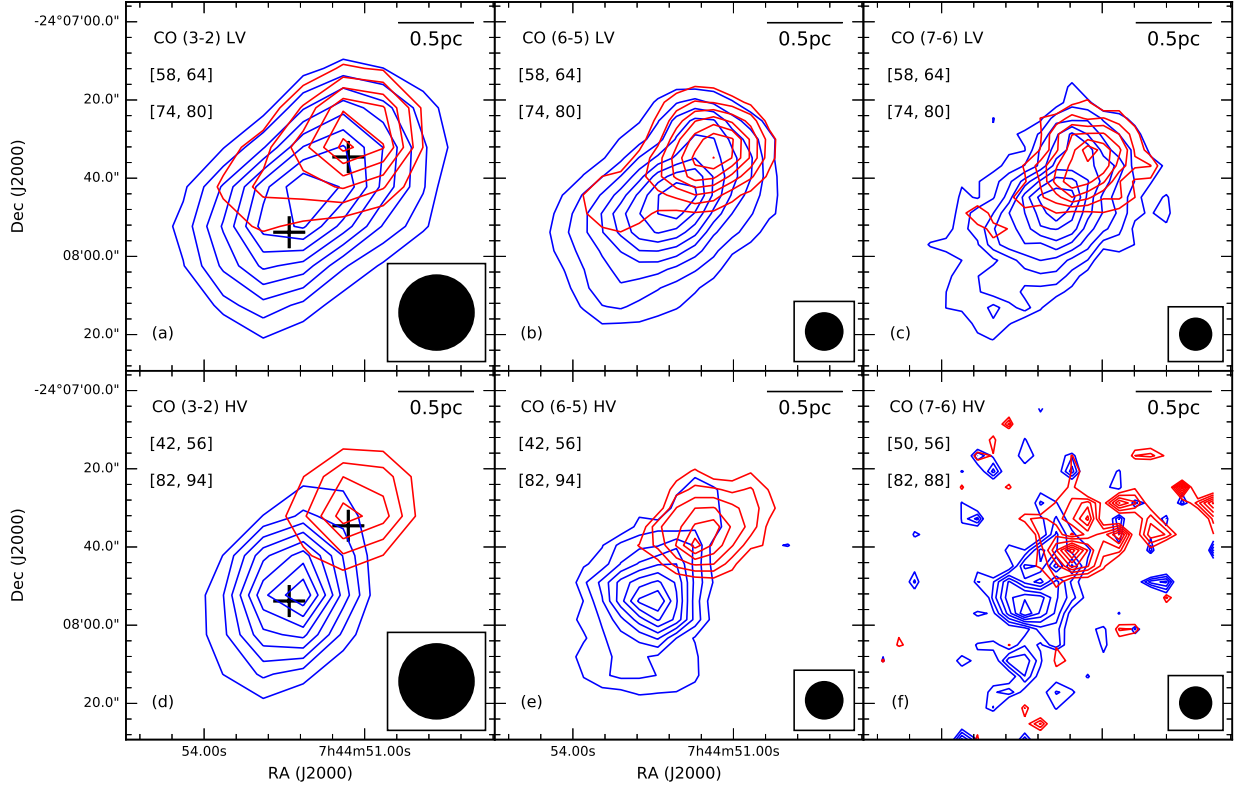


Fig. 1.— (a)-(c) Low-velocity emissions of CO $J = (3-2)$, $(6-5)$, $(7-6)$ lines, integrated from 58 to 64 km s^{-1} and from 74 to 80 km s^{-1} for the blueshifted lobe (blue) and the redshifted lobe (red) respectively; (d)-(e) High-velocity emissions of CO $J = (3-2)$, $(6-5)$ lines, integrated from 42 to 56 km s^{-1} and from 82 to 94 km s^{-1} for the blueshifted lobe (blue) and the redshifted lobe (red) respectively; (f) High-velocity CO $J = (7-6)$ emission, integrated from 50 to 56 km s^{-1} and from 82 to 88 km s^{-1} for the blueshifted lobe (blue) and the redshifted lobe (red) respectively. For (a)-(e), the contour levels start from 20% and continue at steps of 10% of the peak emission. For (f), the contour levels start from 30% and continue at steps of 10% of the peak emission. For (a)-(e), the central stars mark the position of the millimeter sources detected by Qiu et al. (2009). The beam size is shown in the lower right corner of each panel.

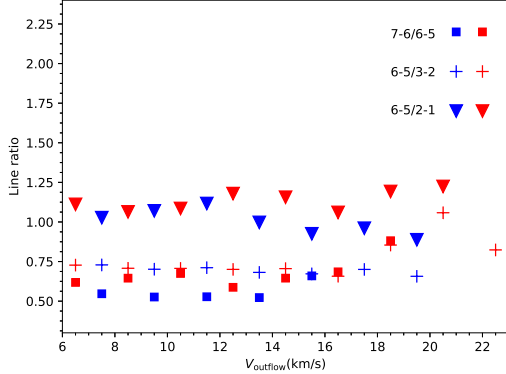


Fig. 2.— Ratios of the main beam temperature of different CO lines versus outflowing gas velocity, as observed towards the blueshifted lobe (blue symbols) and the redshifted lobe (red symbols). The V_{outflow} shown here is the gas velocity with respect to the cloud velocity (v_{cloud}): $V_{\text{outflow}} = |v_{\text{observed}} - v_{\text{cloud}}|$, where v_{observed} is the observed gas velocity.

velocity (v_{cloud}) from Kumar et al. (2003), which is about 67.5 km s^{-1} with respect to the local standard of rest. Figure 2 shows the ratio-velocity distributions of the blueshifted gas and redshifted gas. All line ratios ((7-6)/(6-5), (6-5)/(3-2), (6-5)/(2-1)) appear to be almost constant at different velocities.

3.3. PHYSICAL PROPERTY ANALYSIS

We performed the LVG analysis with the radiative transfer code RADEX developed by van der Tak et al. (2007). The simulation constructs a large grid of non-LTE models with three parameters: gas density (n_{H_2}), kinetic temperature (T_{kin}), and the ratio between column density and line width ($N_{\text{CO}}/\Delta V$). Considering the velocity resolution of our observations, we fix ΔV to 2 km s^{-1} . Each model gives the prediction of the brightness temperature (T_{b}) of different CO transitions. Then we measured the main beam temperature (T_{mb}) of four CO lines extracted at the peak position of the blue lobe and the red lobe (marked as two crosses in Figure 1). So we could compare the simulated T_{b} with our measured T_{mb} , as T_{mb}

is related to T_{b} :

$$T_{\text{mb}} = \frac{\Omega_{\text{s}}^2}{\Omega_{\text{s}}^2 + \Omega_{\text{mb}}^2} \times T_{\text{b}} = f_{\text{b}} \times T_{\text{b}}, \quad (1)$$

where Ω_{s} and Ω_{mb} are the source size and the beam size in arcsec, and f_{b} is the beam filling factor. Given the complex structures of G240 outflow at higher resolution (Qiu et al. 2009), we cannot get a good estimate of the source size. Then the beam filling factors are assumed to be the same for all transitions, and fixed to 1, during our analysis. Thus, the derived physical parameters of the gas are beam-averaged values. We would further discuss how the beam dilution affect our results in the following part of this section.

We report the results from a χ_{red}^2 fitting. χ_{red}^2 is the reduced χ^2 :

$$\chi_{\text{red}}^2 = \frac{1}{N - n} \sum_{i=1}^4 (I_o - I_m)^2 / \sigma^2, \quad (2)$$

where N is the number of observed intensities, n the number of fitted parameters, I_o the observed intensity, I_m the modelled intensity, and σ is the uncertainty of the observed intensity. With four line observations and three simulation parameters, our fitting has one degree of freedom. Considering the calibration error and pointing accuracy of our CO observations, we set the intensity uncertainty of CO (2-1), CO (3-2), CO (6-5), CO (7-6) to 0.15, 0.2, 0.25, 0.3 respectively. The best fit is then obtained by minimizing the χ_{red}^2 between the observed and modelled data using the Levenberg-Marquardt method (Press et al. 1992). However, at velocities where no CO (7-6) emission is detected, the best fit is obtained by minimizing χ^2 instead of χ_{red}^2 . Then we found the best fitting result at most velocities has a χ_{red}^2 less than 1, indicating that we might be a bit conservative at the intensity uncertainty or the real value of degrees of freedom is smaller than one (Andrae et al. 2010). So we divided $(N - n)\sigma^2$ by a appropriate factor to make χ_{red}^2 approach 1 at most velocities. At some velocities, the χ_{red}^2 remains much less than 1 even after our adjustment of intensity uncertainty, which can account for the anomaly high upper limits of gas temperature at these velocities in Figure 4(a).

In Figure 3, we show cuts in the χ_{red}^2 along the $[T, n]$, $[T, N]$, $[n, N]$ planes for 58 km s^{-1} as an

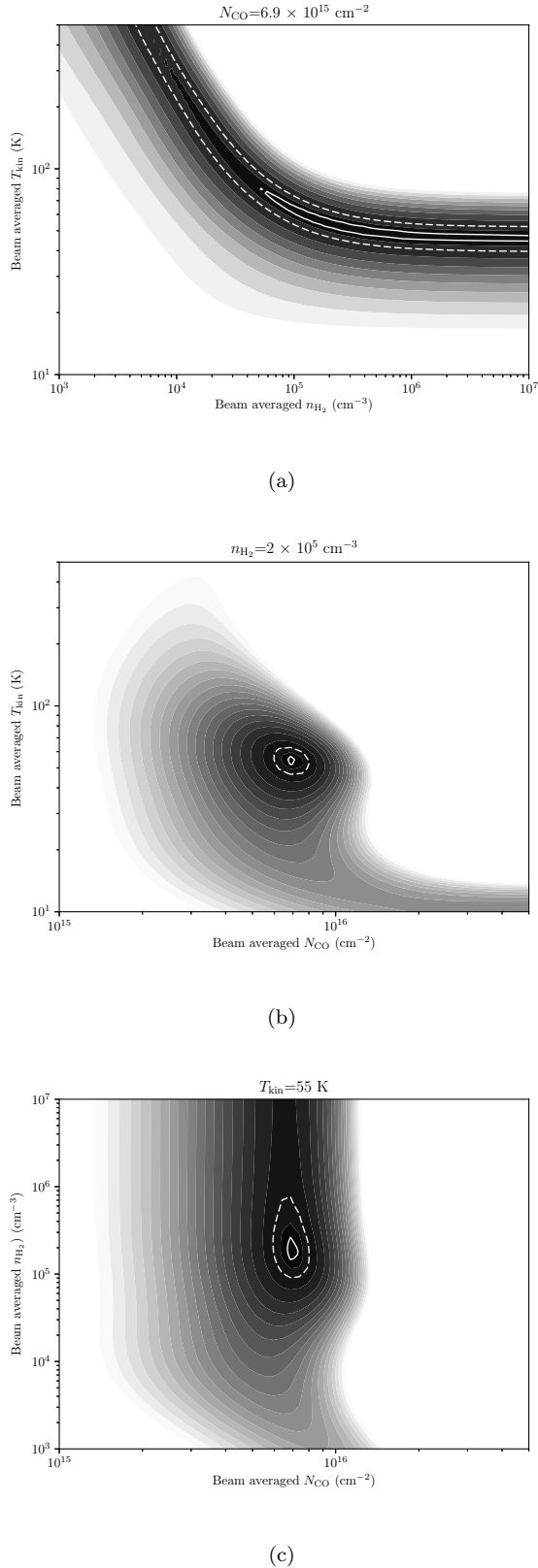


Fig. 3.— The χ^2_{red} distribution for G240 outflow at 58 km s^{-1} in the (a) $[T, n]$, (b) $[T, N]$, (c) $[n, N]$ planes, with all other parameters fixed to the parameters of the best fitting results at this velocity. Solid contours and dashed contours show the 1σ and 3σ confidence levels respectively.

example of the χ^2_{red} distribution, with all the other parameters fixed to the parameters of the best fitting result at this velocity. The χ^2_{red} distribution in $[T, n]$, $[T, N]$ planes is well behaved, with only one minimum, as shown in Figure 3(b) and Figure 3(c). However, Figure 3(a) shows that the gas might be thermalized and no upper limits to the density could be derived. The χ^2_{red} distribution behaves similarly at other velocities.

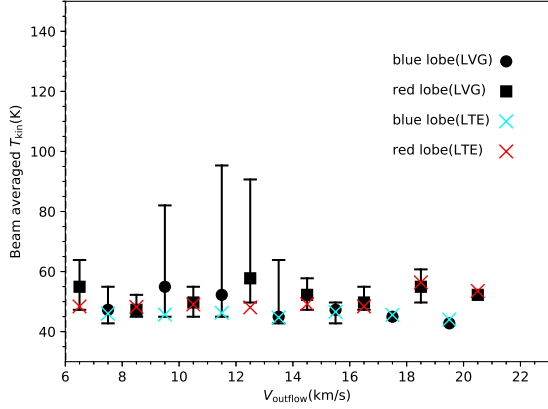
We also performed a population diagram analysis with the assumptions of local thermal equilibrium (LTE) and low opacity, and derived the kinetic temperature of the outflow gas and the CO column density as a function of velocity (Goldsmith & Langer 1999). Figure 4 shows the outflowing gas temperature and CO column density, estimated from the LVG analysis and population diagram analysis, versus outflowing gas velocity. The N - V diagram shows a clear decreasing trend of CO column density with outflow velocity, while the T - V diagram shows that the gas temperature has no obvious dependence on gas velocity. Uncertainty of each parameter in the LVG analysis is derived from the 1σ confidence region in the N - T - n 3-dimensional space. The 1σ temperature uncertainty of the LVG analysis is shown in Figure 4(a), at velocities where all of the four lines are detected. The uncertainty of the CO column density is too small to be plotted, so we don't show it in Figure 4(b). The lower limits of gas density (n_{lower}) are around 10^5 cm^{-3} at most velocities. At velocities where $\chi^2_{\text{red}} \ll 1$, n_{lower} could be as low as $3 \times 10^4 \text{ cm}^{-3}$.

To explore how the effect of beam dilution influence our results, we varied the beam filling factors from 0.2 to 1. Then we performed the LVG analysis again, and compared the simulated T_b with the corrected antenna temperatures (T_{mb} divided by a beam filling factor). We find that modelling with different beam filling factors mainly affect the N - V diagram, with minor change in the T - V diagram and density limits. This could be resulted from the degeneracies of the beam filling factor with CO column density in the optically thin case.

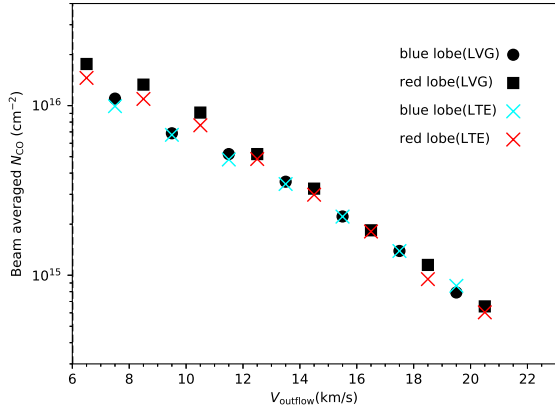
4. DISCUSSION

4.1. Temperature

From the LVG analysis and the population diagram analysis, constant temperatures of $\sim 50 \text{ K}$



(a)



(b)

Fig. 4.— T - V and N - V diagrams of the G240 outflow, estimated from LVG analysis (black circles for blue lobe and black squares for red lobe) and population diagram analysis (cyan x marker for blue lobe and red x marker for red lobe). The 1σ temperature uncertainty estimated from the LVG analysis is represented in the T - V diagram (error bars).

are found for both the blue lobe and red lobe. This value is consistent with temperatures in excess of 50 K probed by van Kempen et al. (2016) for outflows associated with intermediate mass protostars, but slightly lower than temperatures estimated in outflows associated with low-mass protostars (van Kempen et al. 2009; Yıldız et al. 2012).

With priori assumption of other parameters, the kinetic temperature of the outflowing gas can be derived from LVG analysis using two CO lines. Thus, the $T - V$ relation in outflows can be studied. A rising trend of CO 3-2/6-5 ratio is observed towards the outflow gas associated with low-mass YSO HH46 (van Kempen et al. 2009). If the density remains constant, the rising ratios observed at more extreme velocities could correspond to lower kinetic temperatures. In the case of outflowing gas toward low-mass protostars NGC 1333 IRAS 4A and IRAS 4B, the CO 3-2/6-5 ratios are remarkably constant with velocity (Yıldız et al. 2012). With the assumption of constant density, the constant ratio trend shows little or no evidence of a temperature change with velocity. Based on CO (2-1) and CO (3-2) observations towards the extremely high velocity (EHV) outflow of high-mass YSO G5.89-0.39, Su et al. (2012) assumed the canonical CO fractional abundance of 10^{-4} and performed a LVG analysis, revealing an increasing trend of temperature with gas velocity. However, using the CO (6-5), (7-6) and (16-15) lines, Leurini et al. (2015) performed a rotation diagram analysis towards G5.89-0.39 outflow and found a decreasing trend of excitation temperature with increasing velocities. This disagreement seen in results of Su et al. (2012) and Leurini et al. (2015) could be due to different angular resolutions ($3''.4$ compared to $14''.5$). While Su et al. (2012) has smaller energy range covered by their CO line observations ($\Delta E_u \sim 17$ K) compared to $\Delta E_u \sim 600$ K of Leurini et al. (2015), the decreasing trend of temperature with velocity constrained in Leurini et al. (2015) is probably more appropriate for the G5.89-0.39 outflow. The different distributions of temperature with velocity reveal the complexity of molecular outflows.

In the wide-angle wind model, a molecular outflow is the ambient material swept-up by a wide-angle radial wind. In previous numerical works, many authors chose isothermal equations for this model (Li & Shu 1996; Lee et al. 2001). Molecular

cooling dominates the cooling of the shocked material in the outflow at temperatures below 10^4 K (Hollenbach 1997). As the cooling rate increases as n^2 , molecular cooling is very efficient for the density of a wind-driven outflow. Thus, an isothermal state could be reached in a wind-driven outflow, with no temperature change with velocity. This is consistent with our derivation of almost constant temperature in the massive G240 outflow. In addition, some other features of the molecular outflow associated with G240 can also be qualitatively interpreted by the wide-angle wind model (Qiu et al. 2009), while other outflow models have different predictions of these features, as reviewed by Arce et al. (2007). However, most outflow models existed have parameters typical of low-mass outflows. It is necessary to compare the observational results of high-mass outflows with models of similar physical conditions. Statics of outflows associated with high-mass star-forming regions are also essential for us to better understand the driven mechanism of massive outflows and the forming process of high-mass stars.

4.2. Density

The LVG analysis reveals that the lower limits of gas densities are $\sim 10^5 \text{ cm}^{-3}$ at most velocities. We have found a decreasing trend of the beam averaged CO column density ($N_{\text{CO,beam}}$) with gas velocity. As shown in Figure 4(b), for each velocity bin, the beam averaged CO column density drops from $\sim 10^{16} \text{ cm}^{-2}$ to $5 \times 10^{14} \text{ cm}^{-2}$ within 15 km s^{-1} . In the optically thin case, the beam averaged CO column density could be related to gas density n_{H_2} :

$$N_{\text{CO,beam}} = n_{\text{H}_2} \times \Delta V \times \frac{1}{dv/dr} \times X_{\text{CO}} \times f_b, \quad (3)$$

where f_b is the beam filling factor, X_{CO} the CO/H₂ abundance ratio, ΔV the velocity interval and dv/dr is the velocity gradient. A drop in $N_{\text{CO,beam}}$ at more extreme velocities indicates the decrease of one or several of these parameters.

As shown in Figure 3 of Qiu et al. (2009), the source size are $\sim 20''$ and $\sim 10''$ at velocities of $\sim \pm 6 \text{ km s}^{-1}$ and $\sim \pm 20 \text{ km s}^{-1}$ with respect to the cloud velocity, corresponding to beam filling factors of ~ 0.5 and ~ 0.2 , respectively. Considering the 2.5 times drop in the beam filling factor,

the 20 times drop in the beam averaged CO column density is consistent with ~ 8 times decrease in the CO column density. As shown in Shu et al. (1995), estimation from an x-wind model predict the wind density decreasing with velocity and distance from the driving source. Thus, the decrease of gas density could interpret the decrease of CO column density with velocity. Due to the lack of further informations, we cannot assess whether the CO abundance ratio or the velocity gradient has attributed to the drop of CO column density at high velocities.

5. SUMMARY

We have presented a CO multi-transition study towards the molecular outflow of the high-mass star-forming region G240. With the LVG analysis, we have constrained the temperatures to $\sim 50 \text{ K}$ and the H₂ density to values higher than $n \sim 10^5 \text{ cm}^{-3}$. We also find a decreasing trend of CO column density with gas velocity.

REFERENCES

- Andrae, R., Schulze-Hartung, T., & Melchior, P. 2010, arXiv:1012.3754
- Arce, H. G., Shepherd, D., Gueth, F., et al. 2007, *Protostars and Planets V*, 245
- Bachiller, R. 1996, *ARA&A*, 34, 111
- Beuther, H., Schilke, P., Sridharan, T. K., et al. 2002, *A&A*, 383, 892
- Caswell, J. L. 1997, *MNRAS*, 289, 203
- Caswell, J. L. 2003, *MNRAS*, 341, 551
- Chen, H.-R., Su, Y.-N., Liu, S.-Y., et al. 2007, *ApJ*, 654, L87
- Fukui, Y., Iwata, T., Mizuno, A., Bally, J., & Lane, A. P. 1993, *Protostars and Planets III*, 603
- Goldsmith, P. F., & Langer, W. D. 1999, *ApJ*, 517, 209
- Hollenbach, D. 1997, *Herbig-Haro Flows and the Birth of Stars*, 182, 181
- Hughes, V. A., & MacLeod, G. C. 1993, *AJ*, 105, 1495

- Hunter, T. R. 1997, Ph.D. Thesis, 238
- Kumar, M. S. N., Bachiller, R., & Davis, C. J. 2002, *ApJ*, 576, 313
- Kumar, M. S. N., Fernandes, A. J. L., Hunter, T. R., Davis, C. J., & Kurtz, S. 2003, *A&A*, 412, 175
- Lada, C. J. 1985, *ARA&A*, 23, 267
- Lee, C.-F., Stone, J. M., Ostriker, E. C., & Mundy, L. G. 2001, *ApJ*, 557, 429
- Leurini, S., Wyrowski, F., Wiesemeyer, H., et al. 2015, *A&A*, 584, A70
- Li, Z.-Y., & Shu, F. H. 1996, *ApJ*, 472, 211
- MacLeod, G. C., Scalise, E., Jr., Saedt, S., Galt, J. A., & Gaylard, M. J. 1998, *AJ*, 116, 1897
- Maud, L. T., Moore, T. J. T., Lumsden, S. L., et al. 2015, *MNRAS*, 453, 645
- McCutcheon, W. H., Sato, T., Dewdney, P. E., & Purton, C. R. 1991, *AJ*, 101, 1435
- Migenes, V., Horiuchi, S., Slysh, V. I., et al. 1999, *ApJS*, 123, 487
- Press, W. H., Teukolsky, S. A., Vetterling, W. T., & Flannery, B. P. 1992, Cambridge: University Press, —c1992, 2nd ed.,
- Qiu, K., Zhang, Q., Wu, J., & Chen, H.-R. 2009, *ApJ*, 696, 66
- Qiu, K., & Zhang, Q. 2009, *ApJ*, 702, L66
- Qiu, K., Zhang, Q., & Menten, K. M. 2011, *ApJ*, 728, 6
- Qiu, K., Zhang, Q., Menten, K. M., et al. 2014, *ApJ*, 794, L18
- Sakai, N., Nakanishi, H., Matsuo, M., et al. 2015, *PASJ*, 67, 69
- Shepherd, D. S., & Churchwell, E. 1996, *ApJ*, 457, 267
- Shu, F. H., Adams, F. C., & Lizano, S. 1987, *ARA&A*, 25, 23
- Shu, F. H., Najita, J., Ostriker, E. C., & Shang, H. 1995, *ApJ*, 455, L155
- Su, Y.-N., Liu, S.-Y., Chen, H.-R., & Tang, Y.-W. 2012, *ApJ*, 744, L26
- Trinidad, M. A. 2011, *AJ*, 142, 147
- van der Tak, F. F. S., Black, J. H., Schöier, F. L., Jansen, D. J., & van Dishoeck, E. F. 2007, *A&A*, 468, 627
- van Kempen, T. A., van Dishoeck, E. F., Güsten, R., et al. 2009, *A&A*, 501, 633
- van Kempen, T. A., Hogerheijde, M. R., van Dishoeck, E. F., et al. 2016, *A&A*, 587, A17
- Yıldız, U. A., Kristensen, L. E., van Dishoeck, E. F., et al. 2012, *A&A*, 542, A86
- Zhang, Q., Ho, P. T. P., Wright, M. C. H., & Wilner, D. J. 1995, *ApJ*, 451, L71
- Zhang, Q., Hunter, T. R., Brand, J., et al. 2001, *ApJ*, 552, L167